Mechanics of vein, fault and solution surface formation in the Appalachian Valley and Ridge, northeastern Tennessee, U.S.A.: implications for fault friction, state of stress and fluid pressure

GREGORY C. OHLMACHER

Department of Geological Sciences, University of Texas at El Paso, El Paso, TX 79968-0555, U.S.A.

and

ATILLA AYDIN

Rock Fracture Project, Department of Geological and Environmental Sciences, Stanford University, Stanford, CA 94305-2115, U.S.A.

Abstract—Complex patterns of veins, solution surfaces and faults in exposures of the Sevier Shale in the Appalachian fold and thrust belt, Tennessee, U.S.A., result from the interplay between the remote state of stress and stress perturbations caused by slip across thrust faults. In order to gain a better understanding of this interplay and its consequences, a two-dimensional displacement discontinuity boundary-element model (DDBEM) is utilized to interpret structural assemblages from the Sevier Shale. A DDBEM of isolated faults and fault arrays shows that the local state of stress is controlled by the frictional resistance along the faults and the angle between the remote (applied) greatest compressive stress direction and the fault planes. Nowhere is this more evident than within the domains bounded by bed-parallel echelon thrust fault arrays. Here, contrasting structural patterns involving geologically contemporaneous cleavages and bedding-normal veins are recognized. The cleavages are oblique to the trend of the bed-parallel thrust fault arrays implying that the fault arrays were not frictionless during the dissolution process. The bedding-normal veins, however, indicate that the same fault arrays were principal stress planes and nearly frictionless during opening fracturing. Low frictional resistance is interpreted to be due to nearly lithostatic fluid pressures. These contrasting styles are interpreted to result from slip and inter-slip periods of deformation. When the fluid pressure was high, fault friction was low, and the faults slipped. Fracturing dominated the domains between the thrust fault arrays causing the veins to open and a decrease in the fluid pressure. During the inter-slip period the fluid pressure was low; the faults had significant frictional resistance; and pressure solution was the dominant deformation mechanism. The cycling between slip and inter-slip periods and respective states of stress may explain the non-orthogonal relationship between the co-existing veins and cleavages. © 1997 Elsevier Science Ltd.

INTRODUCTION

This paper focuses on the mechanics of formation of the mapped structural assemblages and their implications about the remote and local states of stress, the frictional resistance of the fault planes and fluid pressures during deformation. The veins, which are tensile (dilational or mode I) fractures, and solution surfaces (cleavages), which are anticracks (closing or antimode I; Fletcher and Pollard, 1981), are used to map the principal stress trajectories near mesoscopic thrust faults and normal faults. These inferred natural stress patterns are compared to theoretical stress patterns generated using the two-dimensional displacement discontinuity boundary-element method. Boundary-element models of natural fracture patterns, which are ubiquitous throughout the Appalachians, provide a better understanding and rationalization of the observations and a method for predicting the geometric relationships between various structural elements in places where the whole picture is unavailable. Where available, these geometric relationships can be used to infer possible states of stress acting upon the faults.

This paper examines how slip across and the coefficient of friction, μ, along faults affect the local state of stress around faults, thereby producing contrasting structural assemblages. Theoretical fracture mechanics (Lawn and Wilshaw, 1975; Broek, 1983; Kanninen and Popelar, 1985; Pollard and Segall, 1987) provides analytical solutions to isolated fault (modes II and III) problems in infinite media. Segall and Pollard (1980) used a numerical method based on the analytical solution to examine the effects of echelon fault geometries on the local state of stress. Although their program could solve problems with a variety of applied loading and fault frictions, their paper only examines two applied loading configurations and assumes μ is 0.6 along the fault plane. Erickson and Wiltschko (1991) modeled the changes in the local state of stress along an effectively infinite fault with local variations in shear resistance without defining the physical mechanism that causes the resistance to change. In this study we use the boundary-element method to examine a wide variety of remote loading configurations and various coefficients of friction (shear resistance) for several fault geometries in order to provide details about the perturbation of the local state of stress.

This stress perturbation should lead to the formation of secondary structures in the vicinity of the faults.

The relationship between state of stress and thrust faults first appears in the mechanical paradox, which states that the stress required to overcome the frictional resistance acting along the fault plane is greater than the crushing strength of the rocks within the thrust sheet (Reade, 1908; Smoluchowski, 1909). Hubbert and Rubey (1959) presented a solution to the paradox in which fluid pressure reduces the effective stress acting on the fault plane. Assuming a Mohr–Coulomb failure criterion along the fault with cohesion equal to zero, the frictional (shear) resistance is equal to the effective stress times the coefficient of friction. Reducing the effective stress to zero by, for example, increasing pore fluid pressure to lithostatic stress levels, causes the frictional resistance to approach zero. Thus, thrust sheets are able to move under relatively low differential stress. Consequently, thrust faults with reduced friction in overpressurized areas proposed by Hubbert and Rubey (1959) have the local maximum principal stress trajectory approximately normal to the faults, and secondary structures should record this state of stress. In terranes dominated by strike-slip faults with low frictional resistance, stress orientation indicators show that the local maximum principal stress trajectories are nearly normal to the faults (Mount and Suppe, 1987; Zoback et al., 1987; Rice, 1992). This study, in part using these concepts, addresses an interesting field relationship, non-orthogonal veins and cleavages, and examines the consequences of these results for fluid pressure, dissolution and the state of stress on the faults.

NUMERICAL MODELS OF FAULTS

The displacement discontinuity boundary-element method (Crouch, 1976; Crouch and Starfield, 1983) was used to establish the local state of stress associated with various fault configurations and friction coefficients. The method involves discretizing (subdividing) faults into line segments called patches (Fig. 1). Across each patch is imposed a displacement discontinuity similar to a dislocation, where the displacements on opposite sides of the discontinuity are equal in magnitude but opposite in direction. The analytical solution for a line segment with a constant displacement discontinuity provides the stress field associated with each patch. Since each patch i (Fig. 1) perturbs the stress field throughout the body, it affects the stresses acting on all the other patches, for example patch j. Based on the stress fields for each patch, mathematical relationships can be developed correlating the stresses and displacements of one patch to the stresses and displacements of each of the other patches. These relationships are referred to as 'influence coefficients'. When these coefficients are determined for all the patches, they are assembled into a $2N \times 2N$ matrix, where N is the number of patches and the factor 2
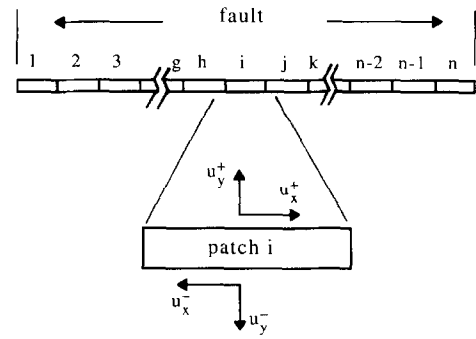

Fig. 1. Discretization of a fracture and the related patch displacements. The boundary element method first subdivides a fracture into N patches. Next, either stresses (σ_x and σ_y) or displacements (u_x and u_y) are prescribed as boundary conditions on each patch. The prescribed stresses or displacements on any patch i will affect the stresses and displacements on any other patch j. By solving all the stress interactions, the local stress field can be found.

represents the shear and normal components of stress and displacement for each patch. Boundary conditions along the patches can either be prescribed displacements or tractions (stresses) associated with each patch. Combining the boundary conditions with the influence coefficient matrix produces a series of $2N$ equations relating tractions or stresses to displacements. These equations are solved using a modified Gauss–Siedel method called 'the method of successive over-relaxation'. Once a solution for these equations is obtained, it can be used to calculate the stresses and displacements at other points in the body.

Overall the boundary-element method provides accurate solutions to fracturing problems. However, one should exercise care when selecting points for calculating the state of stress in the vicinity of a patch. The analytical solution used for the patches has a singularity at each patch end-point (Crouch and Starfield, 1983). Crouch and Starfield report that the solution is accurate at the midpoint of the patch and at distances greater than one patch length away from each patch end-point. For the stress contouring and trajectories presented in this paper, the grid points for calculating stresses were chosen so that they always coincided with the midpoints of the patches, thus, avoiding the singularities at the patch end-points.

The models presented here are interpretive (Anderson and Woessner, 1992, p. 4). Interpretive models are used to analyze the effect of parameter variability on the overall process with or without considering site-specific details. Some site-specific details, for example actual values of material properties, were not considered in our models. Stresses, moduli and cohesion are in systemless compatible stress units. If the readers feel the need, they can apply whatever system stress unit is most comfortable (Pa, GPa, psi, psf, etc.) as long as the same unit is used for all stresses, moduli and cohesions. Stress trajectory measurements are given as angles relative to the fault plane. All changes in stress magnitude and orientation are with respect to the remote (applied) state
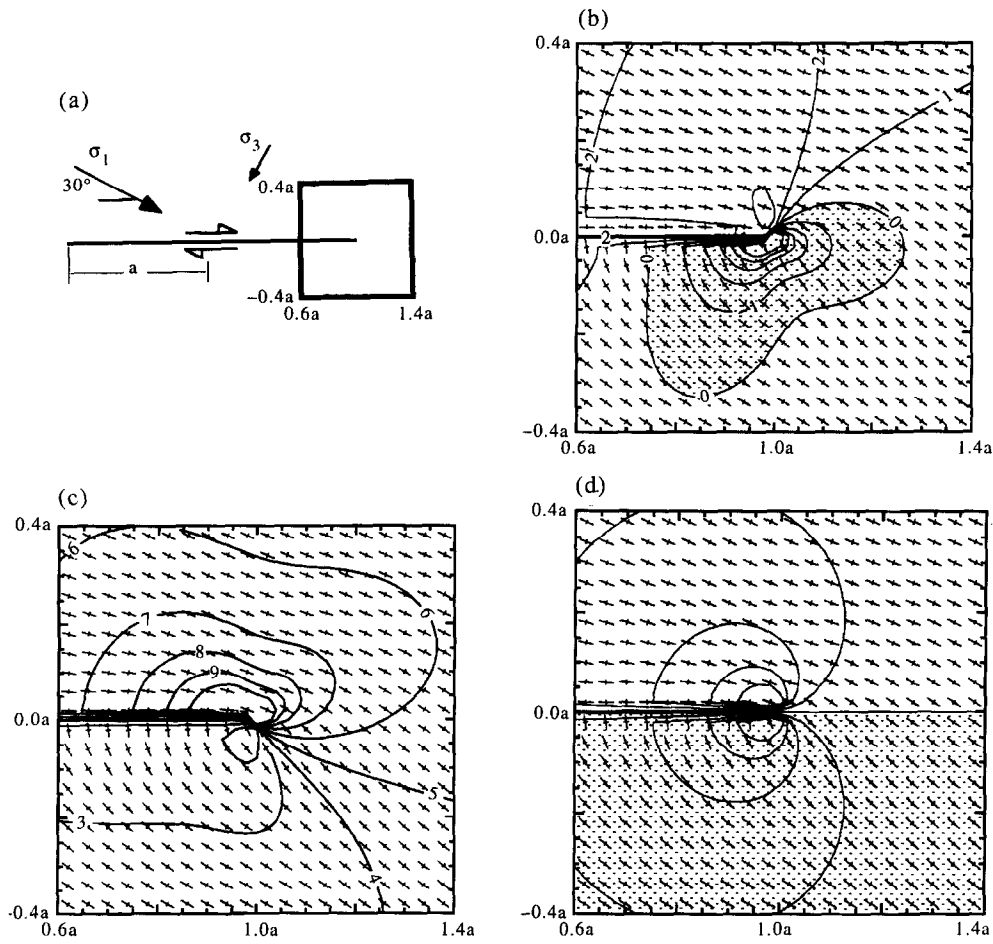
Fig. 2. Plots of the state of stress near the termination of an isolated fault. (a) Plot showing the configuration of the remote loading and the location of the area shown in (b)–(d) relative to the position of the fault. (b) Plot of contours of the magnitude of the minimum principal stress. (c) Plot of contours of the magnitude of the maximum principal stress. (d) Plot of contours of the magnitude of the mean stress. The fault plane is nearly frictionless and the angle to the remote maximum principal stress trajectory, θ_r, is 30°. The shaded areas represent negative stress values for plot (b) and represent mean stress less than 3.0 for plot (d). The crosses in plots (b)–(d) depict the local principal stress trajectories where the long line is the maximum principal stress trajectory and the short line is the minimum. The center of the co-ordinate axes for plots (b)–(d) is located at the midpoint of the fault, and distances are measured in terms of the fault half-length a.

of stress, which would be the state of stress for an infinite body without a slipping fault.

The following conditions apply to all models. The material is assumed to be homogeneous, isotropic, linearly elastic and infinite in extent with a shear modulus of 1.0 and a Poisson's ratio of 0.25. Compression is positive. All models are plane strain. Slip along faults is controlled using a Mohr–Coulomb failure criterion. The cohesion along fault planes is zero. Interpenetration of fault walls, which is a problem with some numerical methods, is prevented by assuming the fault contains a thin layer of material, gouge, with a high stiffness normal to the fault plane. All faults are thrusts with top-to-the-right motion.

Our models investigate the effects of remote stress magnitude and direction, and coefficient of friction, along the fault plane on the orientation of the local stress trajectories. The remote state of stress represents the loading along the outer edge of an 'effectively' infinite body. It should be noted that the use of a perfectly

frictionless fault ($\mu = 0.0$) was avoided because it causes a numerical error in the computer program. Four fault configurations will be considered: an isolated fault; two faults with an extensional stepover; two faults with a contractional stepover; and two parallel faults.

An isolated fault

The simplest case to be examined is that of an isolated mode II fracture. The general features of the local stress field near the fault tip can be seen in Fig. 2. For this model the magnitude of the remote maximum principal stress is 5.0 and its orientation is 30° to the fault, the magnitude of the remote minimum principal stress is 1.0, and the coefficient of friction, μ, is 0.0001 (nearly frictionless). The minimum principal stress contours show a region of tensile stress (negative stress units) below the fault termination (Fig. 2b). This region of tension is referred to as the extensional quadrant of the fault and is where tensile (mode I) fracturing will be favored. On the

opposite side of the fault, the magnitude of the local maximum principal stress increases relative to the remote maximum principal stress (Fig. 2c). This region is the contractional quadrant of the fault, and solution surfaces (anti-mode I) will be favored. These results are compatible with the results of Segall and Pollard (1980) and Pollard and Segall (1987).

The same two quadrants are visible in the mean stress (σ_m) plot (Fig. 2d). The remote mean stress for this model is 3.0. A region where the mean stress is less than 3.0 ($\sigma_m < 3.0$) below the fault plane approximately matches the extensional quadrant in Fig. 2(b). Correspondingly, the region where the mean stress is greater than 3.0 ($\sigma_m > 3.0$) approximately matches the contractional quadrant in Fig. 2(c). As changes in mean stress highlight both the extensional and contractional quadrants, mean stress plots will be used exclusively throughout this paper.

The effect of changing the magnitude of the remote principal stresses on the orientation of the local principal stress trajectories, θ_l, is evaluated with models of isolated faults. For these models, three points were selected (Fig. 3a). All three points are located above the fault at a distance equal to 1.75% of the half length. The first point is located above the left fault tip in the extensional quadrant of the fault; the second is located above the right fault tip in the contractional quadrant; and the third is located above the midpoint of the fault. The first two points were selected because they are close to the singularity in the stresses associated with the fault tips, and the third was chosen to examine the variability in orientation of local stress trajectory along the length of the fault. For all the models both the remote maximum and remote minimum principal stresses are compressive ($\sigma_1 > \sigma_3 > 0$). The angle between the orientation of the remote maximum principal stress trajectory and the fault plane θ_r is 30°, and four coefficients of friction ($\mu = 0.0001$, 0.1, 0.3 and 0.6) are used. The results are presented in terms of remote stress ratio defined as the ratio between the maximum and minimum principal stresses ($\sigma_1 : \sigma_3$).

Holding the remote stress ratio constant and changing the magnitudes of both remote principal stresses has no effect on the orientation of the principal stress trajectories but does affect the magnitudes of these stresses. Varying the stress ratio affects both the orientation and magnitudes of the local principal stresses. A stress ratio of 1:1 is a hydrostatic stress field with no shear stress acting on the fault. In this case θ_l is the same as θ_r, which is 30° to the fault. As the remote stress ratio is changed from 1:1 to about 25:1 an abrupt change in θ_l occurs (Fig. 3b). As the remote stress ratio is increased from 25:1 to greater than 250:1, the rate of change for θ_l decreases and becomes asymptotic to a value unique to each point. A question regarding common stress ratios for fold and thrust tectonism is not evaluated here. However, we assume that the remote stress ratio is at the low end (1:1 to 50:1) rather than at the high end (50:1 to 250:1). For the

remaining models in this paper, a stress ratio of 5:1 will be used. These are the same remote stress magnitudes used by Segall and Pollard (1980) and Aydin and Schultz (1990), and place the models in the markedly changing portion of the graph in Fig. 3(b).

Figure 3(b) also highlights the effect of changes in the coefficient of friction, μ, on the orientation of the local principal stresses. The greatest angular change between θ_l and θ_r at the three points investigated is always for the lowest coefficient of friction regardless of remote stress ratio. For example, at the fault midpoint, θ_l for $\mu = 0.0001$ has rotated from the 30° remote maximum principal stress trajectory to 1.7° (nearly parallel to the fault). For $\mu = 0.6$ at the same point, θ_l is 17.2°. For a coefficient of friction of 0.0001, θ_l markedly changes orientation from a stress ratio of 1:1 to 1.1:1. From 1.1:1 to 250:1, θ_l remains at a relatively constant angle. For a coefficient of friction of 0.6, the rate of change for θ_l relative to the remote stress ratio is high between stress ratios of 1:1 and 25:1. The rate of change is, however, lower for lower coefficients of friction. The orientation of the local principal stress trajectory for a coefficient of friction of 0.6 reaches a relatively constant value at a remote stress ratio of 25:1. Thus, the orientations of the local principal stress trajectories for faults with low coefficients of friction have the highest angular change and reach these values at lower remote stress ratios (near 1.1:1).

The location along the fault is also important to the orientation of the local stress trajectories (Fig. 3b). Above the fault midpoint a difference of more than 15° in θ_l is observed between a fault with $\mu = 0.0001$ and one with $\mu = 0.6$. Secondary structures forming in this region will have a slight but observable orientation difference depending on the coefficient of friction along the fault. However, at both fault tips and at remote stress ratios from 5:1 to 250:1 the difference between the orientation of the local principal stress trajectories at different coefficients of friction is less than 5°. Secondary structures forming in the fault tip areas would have similar orientations at high remote stress ratios.

The orientation of the local stress trajectories also varies depending on the orientation of the remote stress trajectory. For the following models θ_r is changed from 0° to 90° to the fault and θ_l is recorded at the same three points for four coefficients of friction. The remote stress ratio is held constant at 5:1. The results are plotted as three sets of curves relating θ_l to θ_r (Fig. 3c–e). A curve that is below a line with a slope of 1 indicates a decrease in θ_l relative to θ_r (counter-clockwise rotation of the local stress field). A curve above that diagonal indicates an increase in θ_l (clockwise rotation of the local stress field). The greater the distance from the diagonal line, the greater the angular change in θ_l. As with the earlier models the largest change in θ_l is associated with a low coefficient of friction ($\mu = 0.0001$).

A change from clockwise to counter-clockwise rotations of θ_l is observed at all three points. Above the midpoint of the fault this change occurs at $\theta_r = 45°$ (Fig.
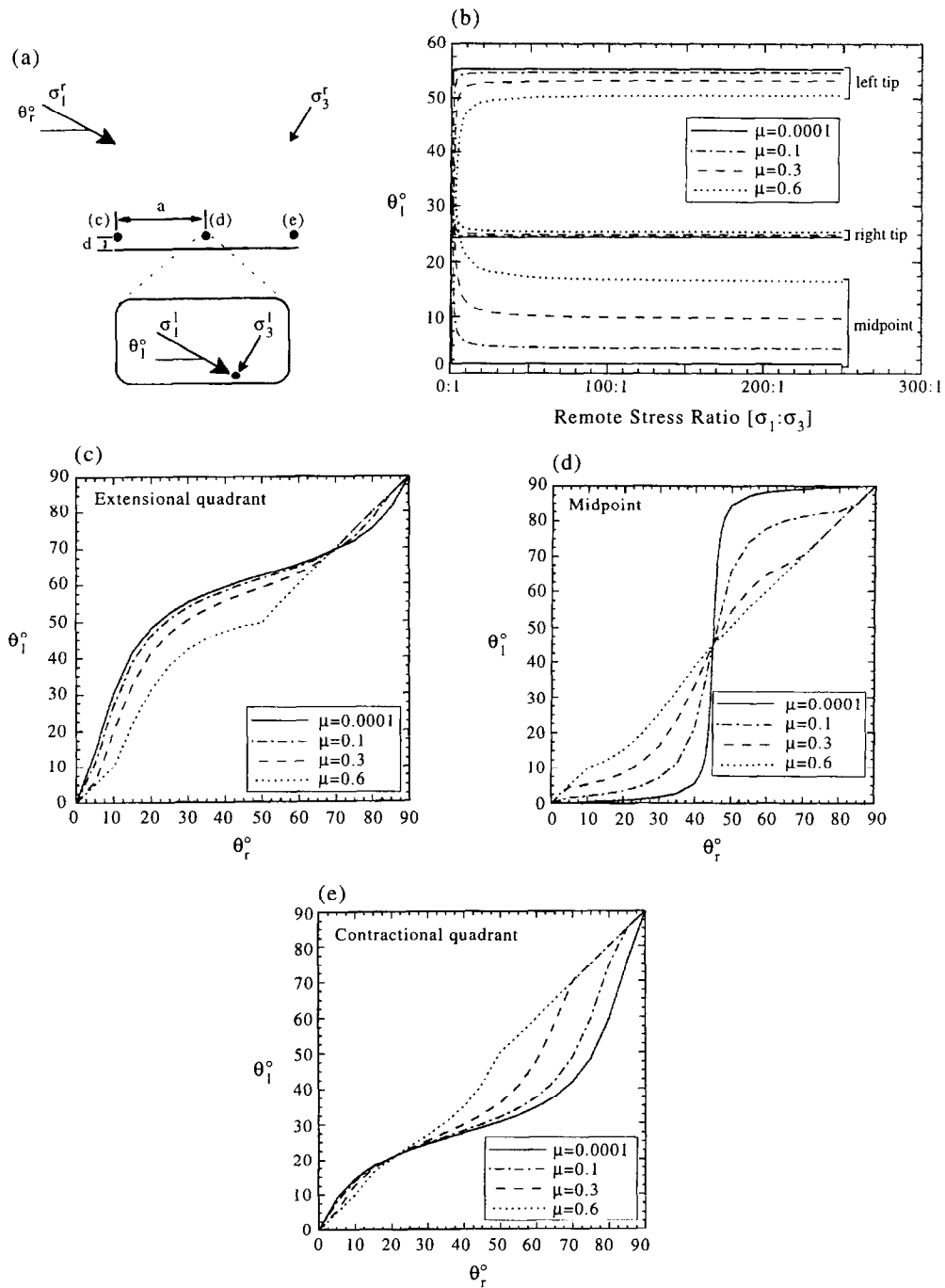
Fig. 3. Graphs showing the effects of remote (applied) stress ratio, orientation of the maximum principal stress trajectory relative to the fault θ_r and the coefficient of friction μ on the orientation of local principal stress trajectory θ_1 for an isolated fault in an 'effectively' infinite medium. (a) Plot showing the configuration of the model with the remote loading and the location of the three points (c–e) where the local stresses are evaluated for plots (c)–(e), respectively. These points are located a distance $d = 0.0175a$ from the fault, where a is the fault half-length. (b) Graph of θ_1 vs the ratio between the magnitude of the remote maximum and minimum principal stresses (remote stress ratio) for four coefficients of friction at the three points shown in (a). The point above the left fault tip is in the extensional quadrant of the fault. The point above the right tip is in the contractional quadrant. (c) Graph of θ_1 vs θ_r for four coefficients of friction above the left tip in the extensional quadrant. (d) Graph of θ_1 vs θ_r for four coefficients of friction above the midpoint. (e) Graph of θ_1 vs θ_r for four coefficients of friction above the right tip in the contractional quadrant. For plots (c)–(e) the greater the deviation a curve has from a diagonal with a slope of 1, the greater the angular change in local stress trajectory. Also, where $\theta_1 > \theta_r$, which is above the diagonal, the rotation of the local stress is clockwise, and where $\theta_1 < \theta_r$, which is below the diagonal, the rotation is counter-clockwise.

3d). For $\theta_r > 45°$, θ_1 is rotated in a clockwise direction; and for $\theta_r < 45°$, θ_1 is rotated counter-clockwise. In the extensional quadrant above the left fault tip the change in θ_1 is from counter-clockwise to a clockwise rotation and

occurs at about 70°, regardless of the coefficient of friction (Fig. 3c). In the contractional quadrant (Fig. 3e), the change is from clockwise to counter-clockwise rotation and occurs at about 20°.
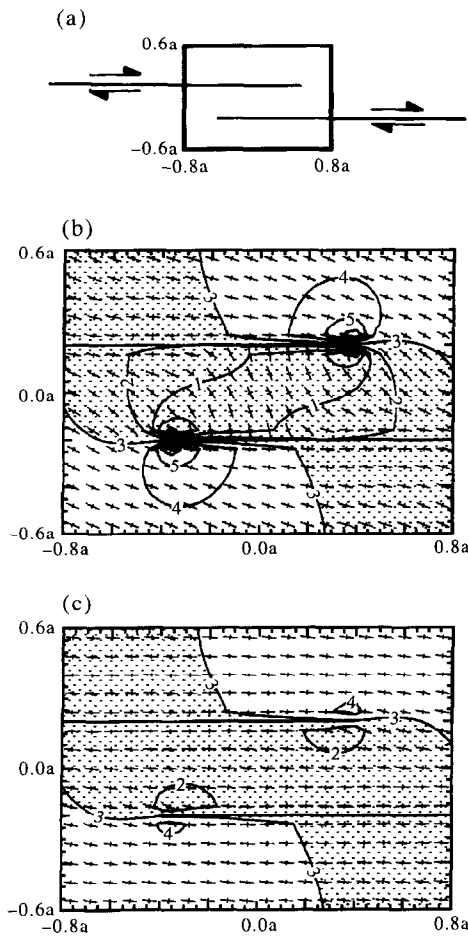
(a)

(b)

(c)

Fig. 4. Plots of the magnitude of the mean stress and local principal stress trajectories for an extensional stepover. In both models $\mu = 0.0001$. Sketch (a) depicts the location of the area in plots (b) and (c) relative to the faults. The center of the co-ordinate axes for plots (b) and (c) is located at the midpoint of the stepover, and distances are measured in terms of the fault half-length a. The crosses in plots (b) and (c) depict the local principal stress trajectories where the long line is the maximum principal stress trajectory and the short line is the minimum. In (b) $\theta_r = 30°$. In (c) $\theta_r = 10°$.

Ranges of remote principal stress trajectories exist where θ_1 remains relatively constant ($\pm 10°$) when the coefficient of friction is 0.0001. Above the midpoint (Fig. 3d) the local maximum principal stress trajectory is subparallel to the fault for $\theta_r < 45°$ and subnormal to the fault for $\theta_r > 45°$. In the extensional quadrant (Fig. 3c) as θ_r increases from $0°$ to $30°$, θ_1 abruptly rises to near $65°$, and then remains relatively constant over a range of θ_r from $30°$ to $70°$. In the contractional quadrant (Fig. 3e), θ_1 plateaus at a value of $25°$ for the range of θ_r from $15°$ to about $50°$.

Echelon fault configurations

Two types of stepovers between echelon faults exist. In the first type the thrust segments step down in the transport direction (Fig. 4a). This is equivalent to right-stepping fault segments along right-slipping faults (Aydin and Nur, 1985; Ohlmacher and Aydin, 1995). In the second type the thrust segments step up in the

transport direction (Fig. 5a), which is equivalent to left-stepping segments along right-slipping faults. Boundary-element models for each configuration are analyzed.

For the stepovers where the thrust segments step down, the magnitude of the mean stress σ_m is less than 3.0 within the stepover region (Fig. 4b & c). This corresponds to a decrease in magnitude of the local minimum principal stress, and tensile fracturing will be favored. Thus, this sense of step is called an extensional stepover. Additionally, the local principal stress trajectories within the stepover region vary with changes in the coefficient of friction along the fault and the orientation of the remote principal stresses. When $\mu = 0.0001$ and $\theta_r = 30°$, the magnitude of σ_m within the stepover region decreases (more tension) and θ_1 increases to about $90°$ at the midpoint of the stepover region (Figs 4b & 6a). Correspondingly, the angle between any tensile fractures forming within stepovers and the bounding faults will increase as the fault friction decreases. As θ_r is decreased to $10°$ with $\mu = 0.0001$, θ_1 decreases becoming nearly parallel to the faults (Figs 4c & 6a). Tensile fractures within this stepover are predicted to be subparallel to the bounding faults. The change from high-angle tensile fractures ($\theta_1 \approx 90°$) to low-angle tensile fractures ($\theta_1 \approx 0°$) for $\mu = 0.0001$ occurs when $\theta_r \approx 24°$ (Fig. 6a).

For the stepovers where the thrust segments step up, the magnitude of σ_m is greater than 3.0 within the stepover region (Fig. 5b–d). These stepovers are referred to as contractional stepovers because of the increased compression. In contractional stepovers, as the coefficient of friction along the fault decreases with $\theta_r = 30°$, the magnitude of σ_m within the stepover region increases ($\sigma_m > 3.0$) and θ_1 decreases ($\theta_1 < \theta_r$; Figs 5b & 6b). Solution surfaces forming within the stepover region will be at high angles to the faults, as is observed in cleavage duplexes (Nickelsen, 1986; Aydin, 1988). As θ_r increases with the fault friction held constant, θ_1 within the stepover region increases ($\theta_1 > \theta_r$; Figs 5 & 6b). Solution surfaces within this type of stepover region are predicted to be subparallel to the bounding faults. The change from high-angle solution surfaces ($\theta_1 \approx 0°$) to low-angle solution surfaces ($\theta_1 \approx 90°$) for $\mu = 0.0001$ is when θ_r is about $67°$ (Fig. 6b). All the results for echelon faults are compatible with numerical models of echelon faults presented by Segall and Pollard (1980).

Two parallel faults

The next series of boundary-element models involves two parallel faults with equal lengths (Fig. 7a). In these models (Fig. 7b–f) θ_r is set at either $30°$ or $60°$ to the faults. Three coefficients of friction along the faults were considered for the stress field plots: $\mu = 0.0001$, $\mu = 0.1$ and $\mu = 0.6$. For the graph comparing θ_1 with θ_r (Fig. 8), a fourth coefficient of friction ($\mu = 0.3$) was also considered. The spacing between the faults is 10% of the fault length a.

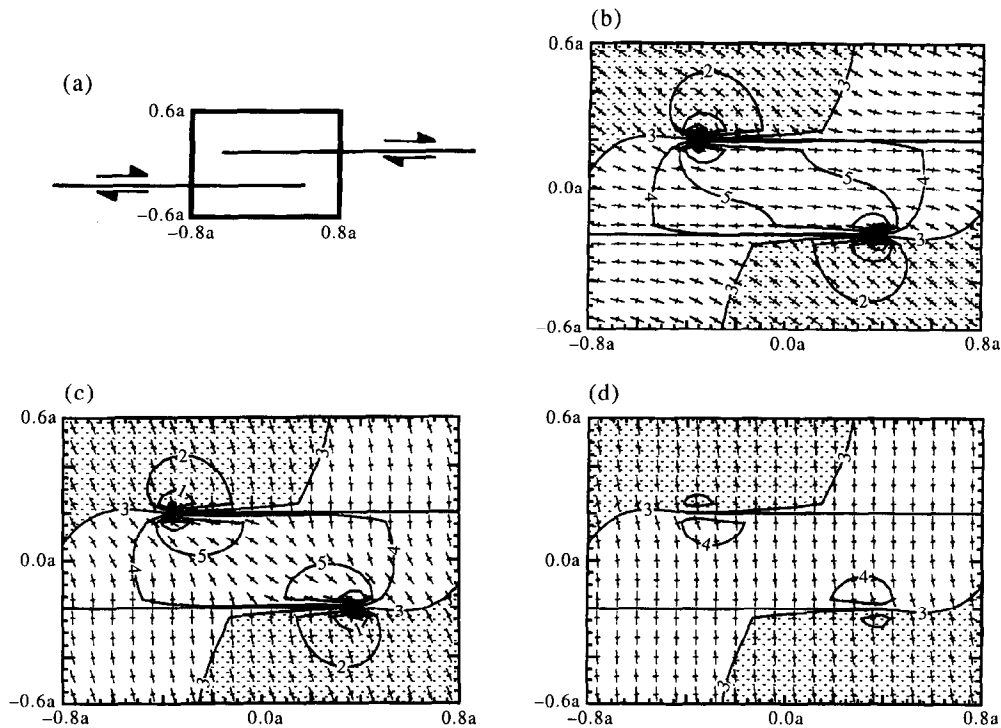All the boundary-element models demonstrate that the

Fig. 5. Plots of the magnitude of the mean stress and the local principal stress trajectories for a contractional stepover. In these models $\mu = 0.0001$. Sketch (a) depicts the location of the area in plots (b), (c), and (d) relative to the faults. The center of the co-ordinate axes for plots (b)–(d) is located at the midpoint of the stepover, and distances are measured in terms of the fault half-length a. The crosses in plots (b)–(d) depict the local principal stress trajectories where the long line is the maximum principal stress trajectory and the short line is the minimum. In (b) $\theta_r = 30°$. In (c) $\theta_r = 65°$. In (d) $\theta_r = 80°$.

orientations of the principal stress trajectories are relatively constant within the domain bounded by the parallel faults. However, near the fault terminations this pattern is affected by the singularities in the stress fields, which is not shown in Fig. 7. The local principal stress trajectories are affected by both the coefficient of friction and the orientation of the remote principal stress trajectories with respect to the faults. For the case with $\mu = 0.6$ and $\theta_r = 30°$, $\theta_1 = 26°$ at the midpoint of the domain between the fault segments (Fig. 7b), there is a 4° counter-clockwise rotation in the stress orientation relative to θ_r. Little or no rotation of the local principal stresses is observed for other remote stress orientations, especially for trajectories greater than 45° (dotted line in Fig. 8). For the case with $\mu = 0.1$ and $\theta_r = 30°$, $\theta_1 = 6°$ (Fig. 7d), there is a 24° counter-clockwise rotation relative to θ_r. With $\theta_r = 60°$, $\theta_1 = 79°$ (Fig. 7c), there is a 19° clockwise rotation relative to θ_r. Two conclusions can be drawn from these models. (1) As the coefficient of friction is lowered, the angular change in θ_1 increases for all θ_r values (Fig. 8). (2) The trajectory of the remote maximum principal stress affects the direction of rotation of the local maximum principal stress trajectory. When θ_r is greater than 45°, θ_1 becomes more fault normal (clock-wise rotation relative to θ_r). When θ_r is less than 45°, θ_1 becomes more fault parallel (counter-clockwise rotation relative to θ_r).

Isolated frictionless faults should be as principal stress planes and not transmit shear stresses across the fault

planes. This can best be seen above the midpoint of an isolated fault (Fig. 3d) where θ_1 is either subparallel or subnormal to the fault when $\mu = 0.0001$. If a domain is bounded by two frictionless faults, then the local stress trajectories within this domain should be parallel and perpendicular to the faults. This can be seen in Fig. 7(e), where θ_r is 60°. The orientation of the local maximum principal stress trajectory and the orientation of any tensile fractures forming in the domain will be perpendi-cular to the faults ($\theta_1 = 90°$). Solution surfaces would form parallel to the fault planes, that is, the orientation of the minimum principal stress trajectory. The local principal stress trajectory has an abrupt change when $\theta_r = 45°$ (Fig. 8). When θ_r is oriented at 30°, θ_1 is parallel to the faults ($\theta_1 = 0°$; Fig. 7f). In this case tensile fractures would be parallel to the faults, and any solution surfaces would form normal to the faults. The results for the midpoint of the domain between the faults (Fig. 8) compare very closely with the results for the point above the midpoint of an isolated fault (Fig. 3d). This indicates that the local state of stress along the fault segments in the parallel fault case are controlling the local state of stress within the domain between the faults.

Summary of model results

Each of the models produces a characteristic pattern of local stress magnitudes and orientations. Decreased mean stress (increased tension) is associated with the
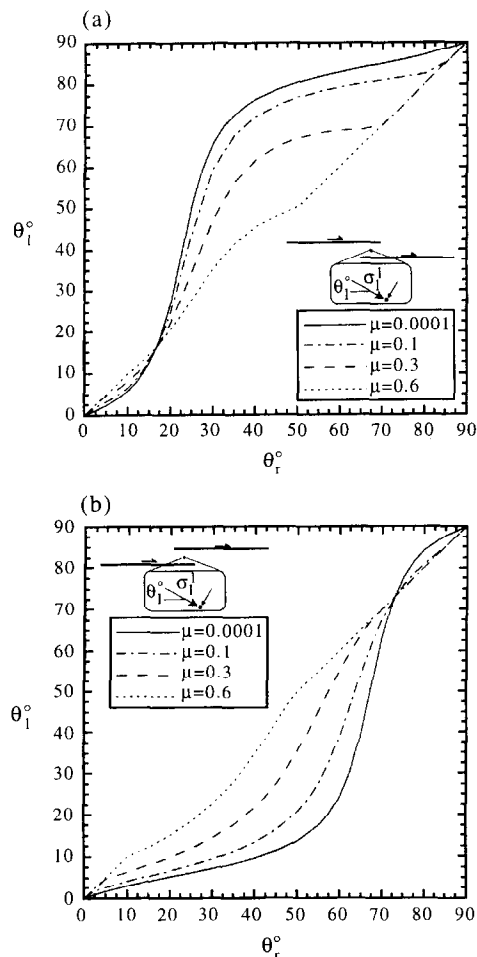
Fig. 6. Graphs showing the effects of orientation of the maximum principal stress trajectory relative to the fault θ_r, and the coefficient of friction μ on the orientation of local principal stress trajectory θ_l for an extensional stepover (a) and a contractional stepover (b). The points where local stresses are evaluated are located at the center of the stepover region—see inset to graphs (a) and (b). Four coefficients of friction were used ($\mu = 0.0001, 0.1, 0.3$ and 0.6).

extensional quadrants of isolated faults and within extensional stepovers, and will increase the likelihood of tensile fracture formation. Increased mean stress (increased compression) will inhibit tensile fracture formation, yet increase the susceptibility to pressure solution in the contraction quadrants of faults and in contractional stepovers. Furthermore, changing the orientation of the remote principal stresses with respect to the faults and the coefficient of friction along the faults affects the pattern of local stress trajectories for each fault configuration modeled. For each coefficient of friction modeled, the largest change in orientation of the local stress trajectories is associated with the lowest coefficient of friction along the faults. The results of the modeling will now be compared with the structures studied in outcrops from the southern Appalachian fold and thrust belt.

GEOLOGICAL SETTING

Structures exposed in highway cuts along Interstate

181–U.S. Route 23 at Bays Mountain, Kingsport, Tennessee and along U.S. Route 19E at Holston Mountain, Elizabethton, Tennessee (Fig. 9a) were mapped in detail (Ohlmacher and Aydin, 1995). The structure of this region is dominated by a series of stacked thrust sheets and large-wavelength folds (Rodgers, 1949, 1970; Harris and Milici, 1977). The Bays Mountain location is within the Saltville thrust sheet. The lower boundary of this thrust sheet is the Saltville thrust and the upper boundary is the Pulaski thrust (Fig. 9b). The Bays Mountain syncline, which is exposed at the site, is a major fold with a wavelength of 2–3 km (Rodgers, 1970). The Holston Mountain location is within the Pulaski thrust sheet. This site is within a set of 1–2-km wavelength regional folds, and the surface trace of Holston Mountain thrust is about 0.7 km to the southeast. Balanced cross-sections by Kulander and Dean (1986) place the Pulaski thrust about 3 km below the site. The only geological unit exposed at both locations is the Sevier Shale, which is thinly bedded (cm) with alternating layers of calcareous shale and siltstone.

KEY FIELD RELATIONSHIPS

The highway cuts mentioned above expose structural assemblages composed of veins, solution surfaces, folds and faults. Detailed field mapping has revealed a complex deformation sequence having seven recognizable stages: (1) early thrust faulting; (2) folding; (3) intermediate thrust faulting; (4) intermediate folding; (5) normal faulting; (6) strike-slip faulting; and (7) jointing. Each of these stages contains one or more structures including veins, solution surfaces, faults and folds. A complete description of these deformation stages and associated structures can be found in Ohlmacher and Aydin (1995). Also note that both Ohlmacher and Aydin (1995) and this paper use a geometric and genetic classification of the structures. The correlation between this classification and existing terminology is included in both papers. From the seven stages, we selected the faults along with secondary veins and cleavages from Stages 1, 3 and 5 to compare with the modeling results in order to gain a better understanding of the remote state of stress and friction along the faults during deformation. Although the assumptions in the models are not an exact match for conditions in the field, we feel that our comparisons still provide valuable insight into the deformation process.

Stage 1. Early thrust faulting and associated structures

The earliest structures observed at both locations are short (cm–m) thrust faults slightly oblique (<20°) to the bedding (Fig. 10a). These thrust faults are primarily observed within the shaley layers. Some thrust faults were active over several deformation stages and have displaced structures associated with Stage 5. Horsetail cracks are tensile fractures at the thrust fault terminations (Fig.
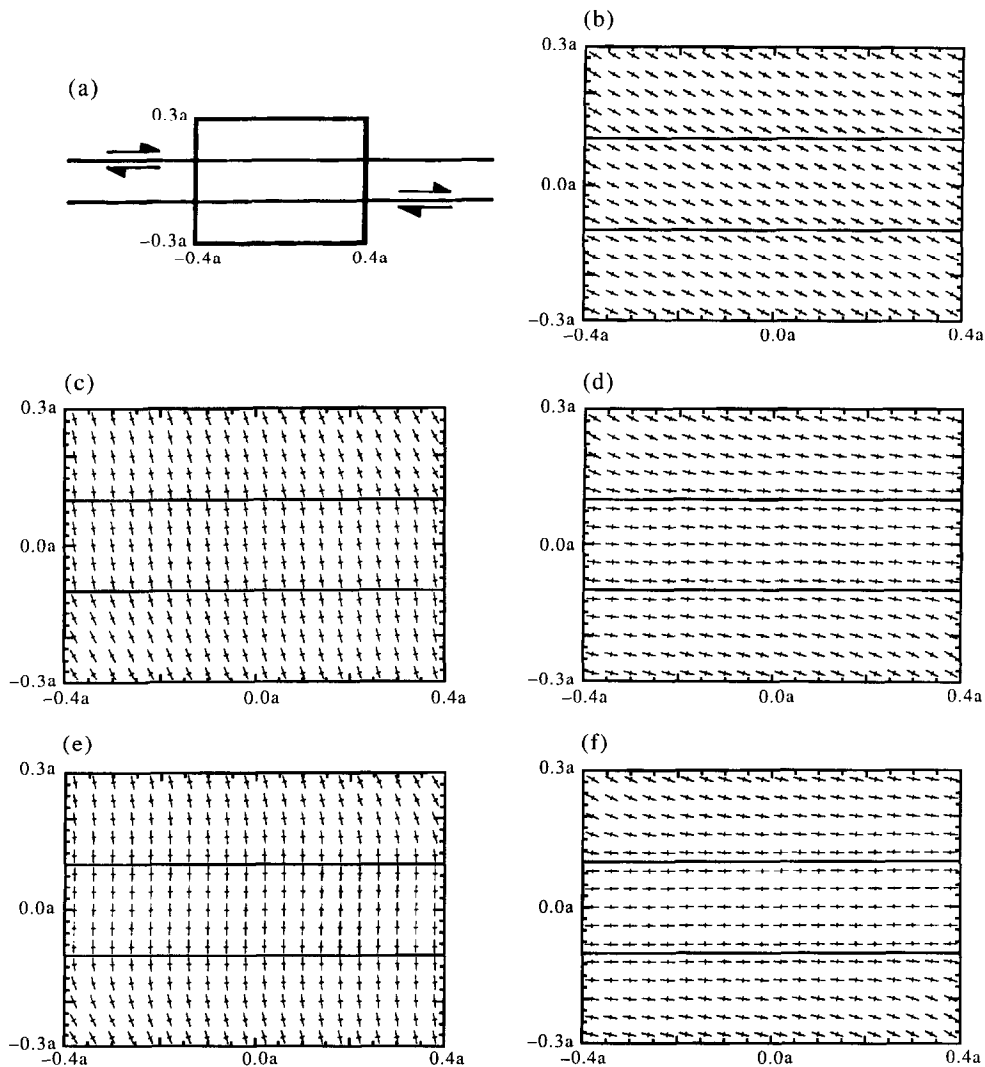
Fig. 7. Plots showing the local principal stress trajectories for models with two parallel faults. Sketch (a) depicts the location of the area in plots (b)–(f) relative to the faults. The center of the co-ordinate axis for plots (b)–(f) is located at the midpoint of the domain bounded by the parallel faults, and distances are measured in terms of the fault half-length a. The crosses in plots (b)–(f) depict the local principal stress trajectories where the long line is the maximum principal stress trajectory and the short line is the minimum. (b) In this case $\mu = 0.6$ and $\theta_r = 30°$. Only a slight rotation of θ_l is observed. (c) $\mu = 0.1$ and $\theta_r = 60°$. The rotation of θ_l relative to θ_r is more noticeable and is shifted toward being more fault normal. (d) $\mu = 0.1$ and $\theta_r = 30°$. Here, the shift of θ_l is more fault parallel. (e) $\mu = 0.0001$ and $\theta_r = 30°$. The local maximum principal stress trajectory is now normal to the fault planes. (f) $\mu = 0.0001$ and $\theta_r = 30°$. The local maximum principal stress trajectory is now parallel to the fault planes.
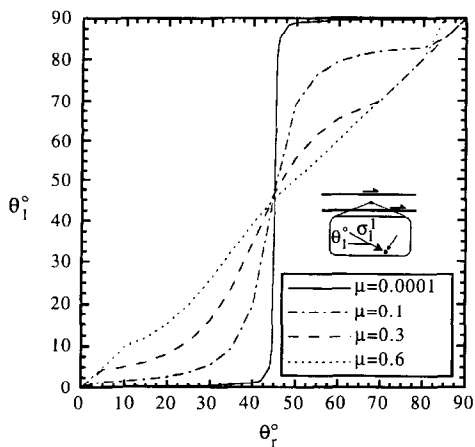

Fig. 8. Graph of the orientation of the local maximum principal stress trajectory θ_l vs the orientation of the remote maximum principal stress trajectory θ_r for four coefficients of friction along the faults ($\mu = 0.0001$, 0.1, 0.3 and 0.6). This two parallel fault case measures the local stress trajectory at the midpoint of the domain bounded by the faults.

10a). On the opposite side of the thrust faults, horsetail solution surfaces (Fletcher and Pollard, 1981) are solution surfaces that are fault-subparallel near the faults and curve to higher angles away from the faults (Fig. 10a).

The thrust fault segments interacted to form two types of echelon arrays in a manner analogous to fault segments along strike-slip faults (Aydin and Nur, 1985) and along thrust faults (Aydin, 1988). One array configuration has consistent down-stepping thrust faults in the direction of transport (Fig. 10b). In the outcrops these arrays trend roughly parallel to bedding. The stepover regions feature tensile fractures connecting the fault segments creating rhombohedral-shaped cavities and are referred to as extensional stepovers or pull-aparts (Ohlmacher and Aydin, 1995, fig. 4). With continued slip the discrete pull-aparts overlap, forming multilayer veins

(a)

(b)

no vertical exaggeration
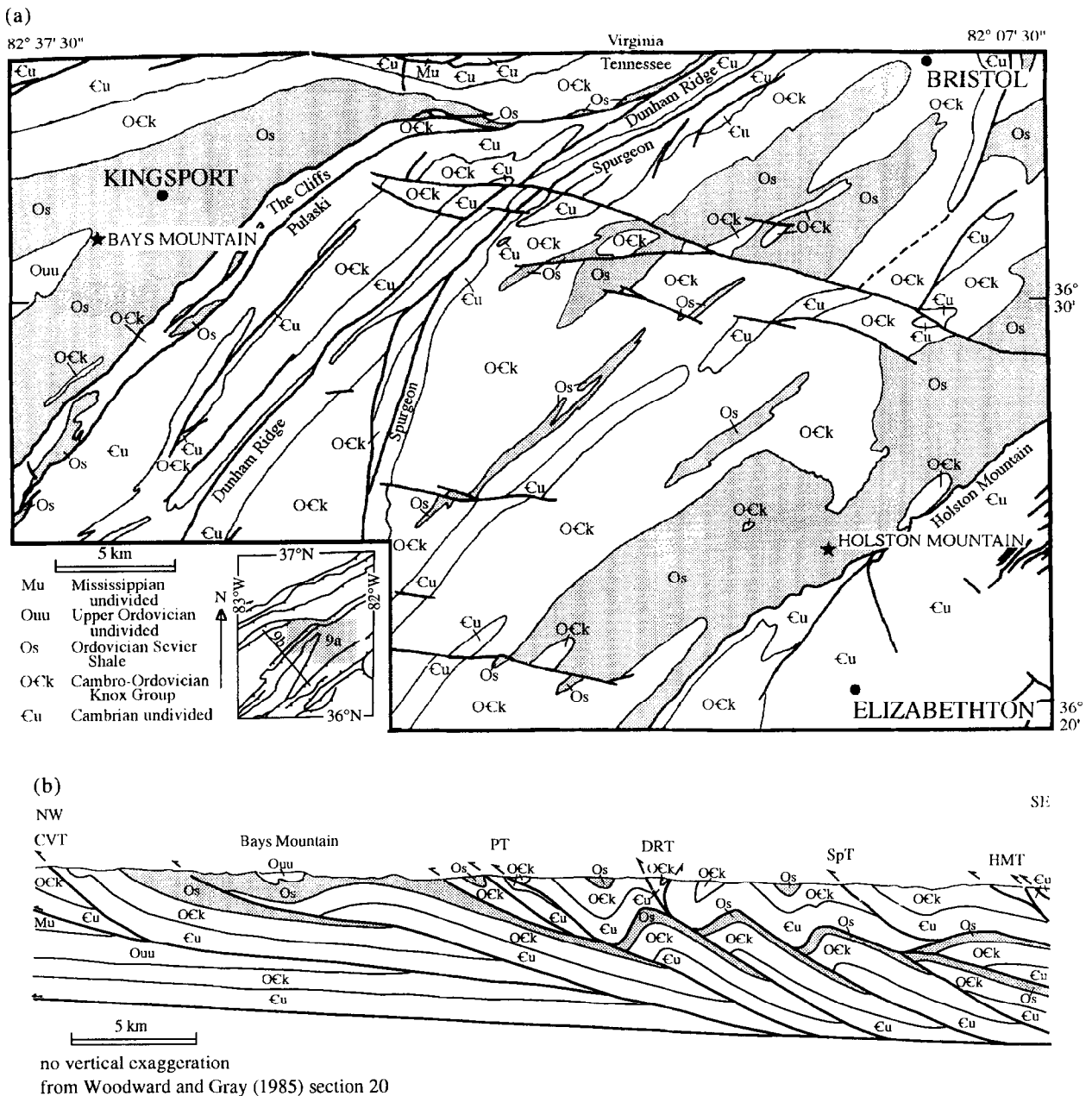from Woodward and Gray (1985) section 20

Fig. 9. Generalized geologic map (a) (after Rodgers, 1953) and cross-section (b) of northeastern Tennessee. Stars mark the outcrop locations. Shaded areas are underlain by the Sevier Shale. Map in the lower left-hand corner of (a) depicts the major faults in the 1° × 1° area encompassing the study area. It also shows the location of map (a) and cross-section (b).

referred to as composite pull-apart veins, which are similar to shear fiber veins (Ramsay and Huber, 1983) and bed-parallel veins (Jessell et al., 1994). The spacing between bed-parallel echelon thrust fault arrays with composite pull-apart veins is variable, ranging from centimeters to decameters.

The second array configuration has consistent up-stepping thrust faults in the direction of transport (Fig. 10c) (Ohlmacher and Aydin, 1995, fig. 8). These arrays trend oblique to bedding. The stepover regions feature solution surfaces connecting the fault segments and are thus called contractional stepovers. In the center of the stepover region the solution surfaces are oriented at high

angles (40–50°) to the faults and curve to become parallel to the faults at the stepover boundaries (Fig. 11a). Parallel echelon thrust fault arrays with contractional stepovers are very closely (mm–cm) spaced and form the observed cleavage.

Bedding-normal veins formed within domains bounded by bed-parallel echelon thrust fault arrays (Figs 10 & 11b). Bedding-normal veins are tensile (pure mode I) fractures because: (1) the intersections of bedding planes and the vein walls on opposite sides of the vein show no shear displacements; and (2) the presence of a few fibers in the vein fill (Fig. 11c). Bedding-normal veins have a morphology similar to ladder veins (De Paor
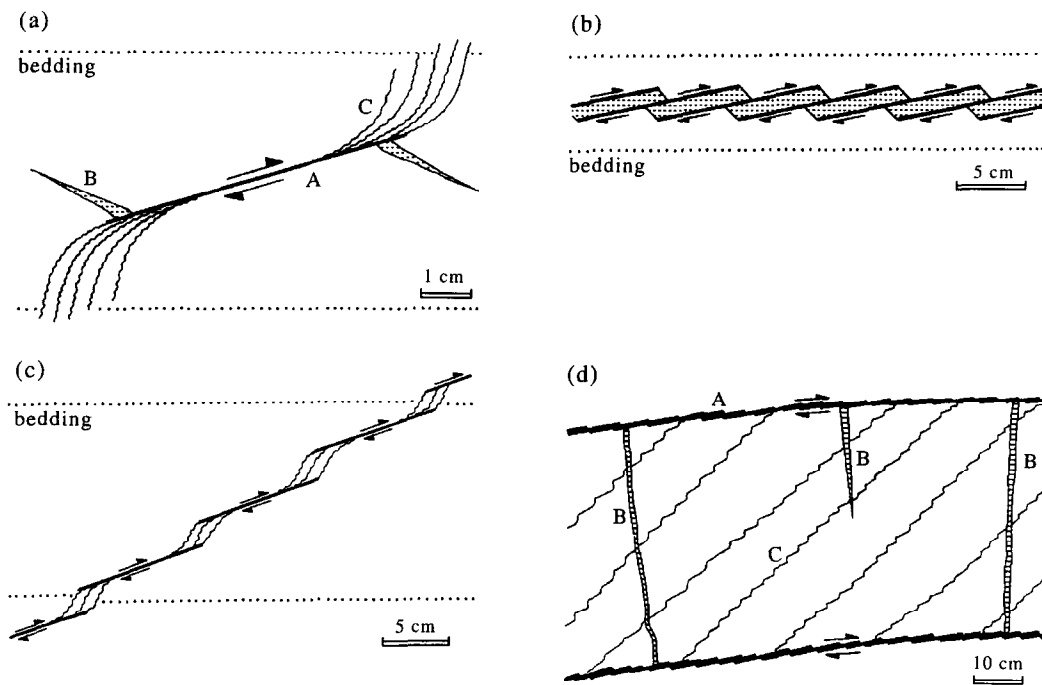
(a)

(b)

(c)

(d)

Fig. 10. Sketches depicting structures related to Stage 1 early thrust faulting. (a) Thrust fault A with horsetail cracks B in the extensional quadrant and horsetail solution surfaces C in the contractional quadrant. (b) Array of echelon thrust faults (thick lines with arrows) connected by pull-aparts (shaded areas) forming a composite pull-apart vein. (c) Array of echelon thrust faults connected by contractional stepovers containing pressure-solution surfaces (wavy lines) that form the cleavage. (d) A domain bounded by bed-parallel echelon thrust fault arrays with associated composite pull-apart veins A. The domain contains bedding-normal veins B and cleavage C. This sketch depicts the non-orthogonal relationship between the bedding-normal veins and cleavage. Dotted lines in sketches (a)–(c) represent bedding.

et al., 1991). The normals to the bedding-normal veins are roughly parallel to slickenlines along the thrust faults. Field evidence including the observations that: (1) bedding-normal veins transect some pull-aparts and connect to a pull-apart within a bed-parallel echelon thrust fault array; (2) the greatest aperture for the bedding-normal veins is within the bed-parallel echelon thrust fault array and the aperture decreases as one follows the bedding-normal vein away from the thrust fault array; and (3) extensions of these bedding-normal veins cannot be found outside the domain bounded by the echelon thrust fault arrays (Ohlmacher and Aydin, 1995, figs 8 & 11) indicate that the bedding-normal veins are contemporaneous with the slip along the bed-parallel echelon thrust fault arrays. Combining the orientation of the veins relative to the slip direction along the faults with the mode of fracture, the extension direction within the domain bounded by the bed-parallel thrust fault arrays indicated by the bedding-normal veins was approximately parallel to the slip direction, or, in other words, the rocks were extended parallel to the transport direction. Field evidence including the observation that bedding-normal veins cut the cleavages and are cut by the cleavages (Ohlmacher and Aydin, 1995, fig. 8) also indicates that the bedding-normal veins and the cleavages occur as alternating events that are, in a geological sense, contemporaneous. However, as the veins and cleavages are not orthogonal, both structures cannot form under the same state of stress.

Stage 3. Intermediate thrust faulting and associated structures

Intermediate thrust faults (Fig. 12) cut and displaced the Stage 2 folds and earlier structures (Ohlmacher and Aydin, 1995, figs 13 & 14). Stage 3 fault-normal veins formed between parallel intermediate thrust faults and are akin to Stage 1 bedding-normal veins.

Stage 5. Normal faulting and associated structures

Fifth stage normal faults (Fig. 11d) are distributed throughout the north outcrop at Bays Mountain and throughout all the outcrops near Holston Mountain. These normal faults occur in conjugate sets and strike parallel to the regional trend of the folds and larger thrust faults. Field relationships indicate that some intermediate thrust faults continued to slip during normal faulting and may bound domains containing normal faults (Ohlmacher and Aydin, 1995, fig. 18).

Normal-fault-subparallel veins (Fig. 13) are tensile fractures observed along the normal faults and between the closely spaced normal faults. These veins include sets of gash and pinnate veins, along with veins that are parallel to the normal faults. Normal-fault-subparallel veins strike parallel to the normal faults, and dip from subparallel to slightly oblique ($<24°$) to them.
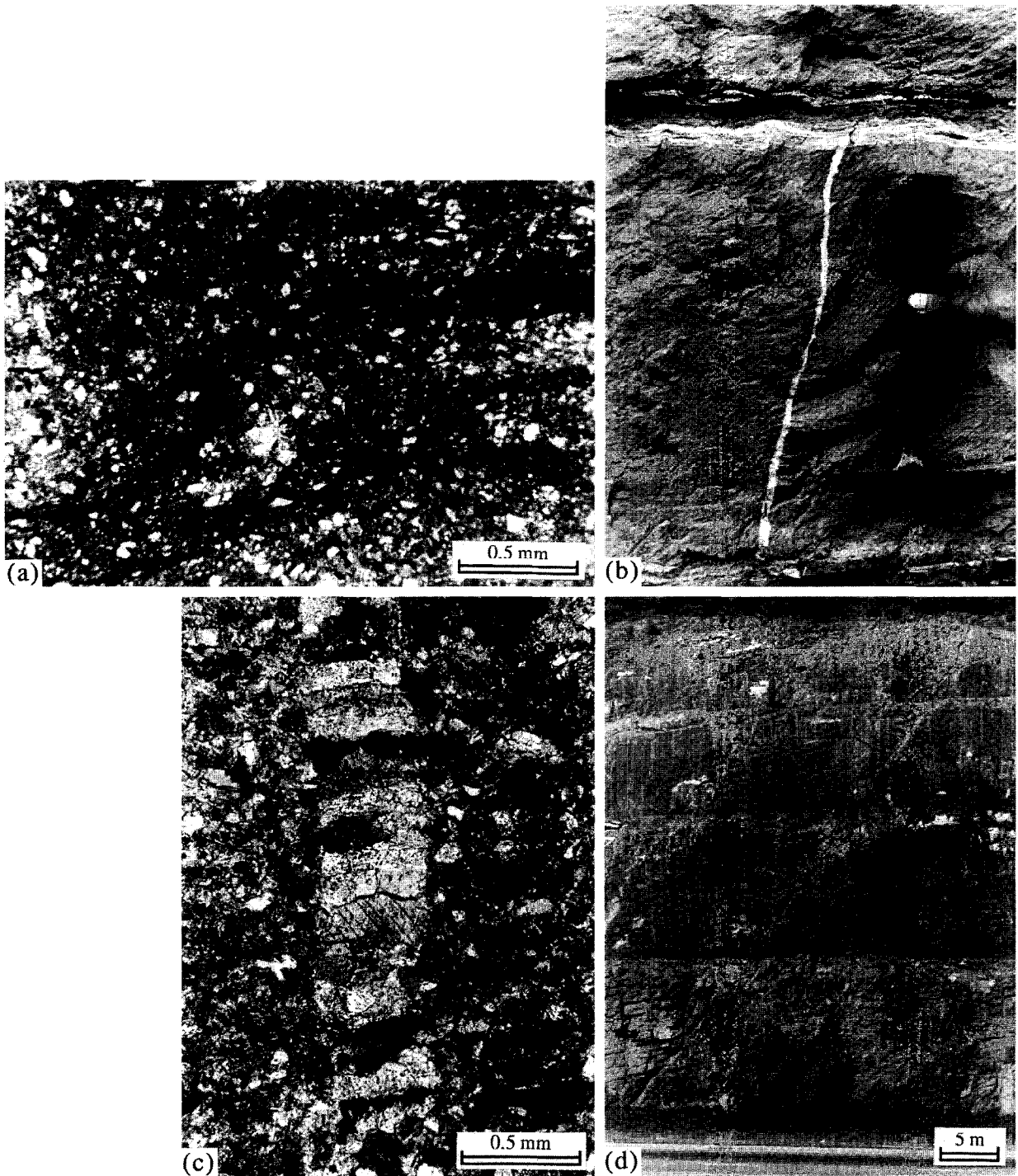
Fig. 11. Photographs and photomicrographs of key structures from the study areas at Bays and Holston Mountain. (a) Photomicrograph of a contractional stepover between echelon thrust faults. Thin dark bands that parallel the upper and lower edges of the photograph are thrust faults, and dark zones that are diagonal to the edges are solution surfaces. (b) Photograph of Stage 1 bed-parallel echelon thrust fault arrays with associated composite pull-apart veins, which are the horizontal veins at the top and bottom of the photograph. These thrust fault arrays bound a domain containing a bedding-normal vein (vertical vein) and cleavage, which extend from the upper right to the lower left. (c) Photomicrograph of a Stage 1 bedding-normal vein in a siltstone layer with calcite fibers perpendicular to the vein walls. Less than 5% of the fill of the bedding-normal veins is fibrous. The remaining vein fill is sparry calcite. (d) Photograph of a Stage 5 normal fault from Bays Mountain. The fault transects the entire outcrop from the upper right to the lower left of the photograph.

COMPARISONS OF THE MODEL RESULTS WITH THE FIELD RELATIONSHIPS

The field observations provide several interesting structural patterns that can be compared to the modeling results. Horsetail cracks and horsetail solution surfaces are associated with slip along the early thrust faults. The echelon thrust fault arrays provide two structural
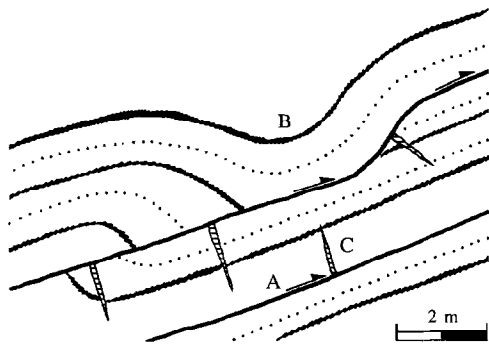
Fig. 12. Sketch depicting structures related to Stage 3 intermediate thrust faulting. Intermediate thrust faults A transect Stage 2 folds and some of the earlier bed-parallel echelon thrust fault arrays B (see Fig. 10b). Fault-normal veins C also form as part of Stage 3. Dotted lines represent bedding.
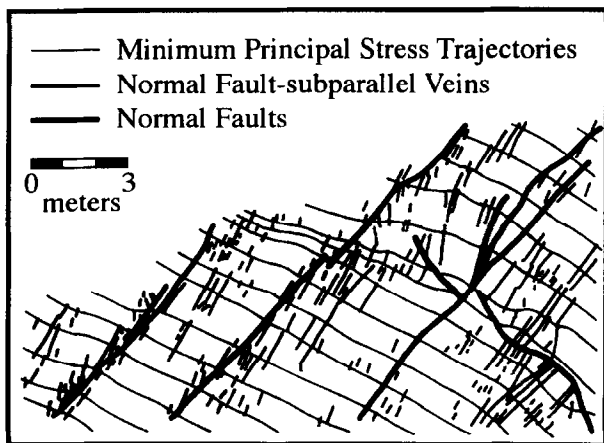

Fig. 13. A detailed cross-section of an area with normal faults and normal-fault-subparallel veins. The thin lines show the trajectories of the minimum principal stress inferred from the veins. Note that these trajectories are approximately perpendicular to the fault planes.
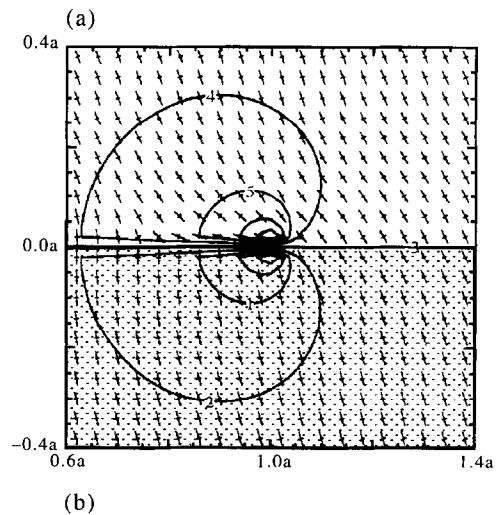

(a)

(b)

Fig. 14. (a) Plot of the magnitude and local principal stress trajectories in the tip region of an isolated fault with $\mu = 0.0001$ (see Fig. 2a for model configuration). The angle to the remote maximum principal stress trajectory is 70°. (b) Sketch of what the pressure-solution surfaces should look like based on this model.

patterns: calcite-filled pull-aparts in extensional step-overs; and solution surfaces in contractional stepovers. Some veins formed within domains bounded by parallel faults including Stage 1 bedding-normal veins, Stage 3 fault-normal veins and Stage 5 normal-fault-subparallel veins. Finally, the Stage 5 normal faults may have formed between parallel intermediate thrust faults.

The results of the numerical models are in good agreement with the field observations of the structural assemblages mapped in Tennessee. Horsetail cracks, for example, are found in regions of reduced mean stress in the extensional quadrants of isolated fault terminations, and horsetail solution surfaces are found in the contractional quadrants (compare Figs 2 & 10a). Numerical models of echelon faults where the thrust faults step down in the transport direction have reduced mean stresses within the stepovers compatible with tensile fracturing and pull-apart formation (compare Figs 4b & 10b). Increased mean stress occurs within the stepovers where the thrust faults step up in the transport direction. Solution surfaces would form within these contractional stepovers (compare Figs 5b & 10c). More information

about the state of stress can be obtained by comparing the detailed stress patterns of the numerical models with: (1) the curvature of solution surfaces; (2) the orientation of tensile fractures and solution surfaces between bed-parallel echelon thrust fault arrays; and (3) the normal faults between parallel intermediate thrust faults.

The orientations of solution surfaces forming at isolated fault terminations and within contractional stepovers can be predicted by plots of the minimum principal stress trajectories. A plot of stress trajectories and magnitudes for the termination region of an isolated fault where $\theta_r = 70°$ and $\mu = 0.0001$ is shown in Fig. 14(a). A sketch of the possible solution surface pattern predicted by this model shows the curvature of the solution surfaces from nearly fault parallel to higher angles toward the fault termination (Fig. 14b). This pattern is a good match for the horsetail solution surfaces observed in thin sections. The local stress pattern for an isolated fault with $\theta_r = 30°$ and $\mu = 0.0001$ is not a match (Fig. 2d). To obtain the stress pattern in Fig. 14(a) the following must be true: (1) θ_1 at the midpoint (right-hand side of Fig. 14a above fault) must be approximately 90°; (2) θ_1 above the fault tip in the contractional quadrant (center of Fig. 14a above fault) must be less than 40°; and (3) μ must be approximately 0.0001. Applying these three criteria to the plots of θ_1 vs θ_r for the midpoint (Fig. 3d) and the contractional quadrant (Fig. 3e) of an isolated fault, θ_r must range from 45° to about 70°.

Solution surface curvature is also observed in contractional stepovers (Fig. 11a). An almost perfect match for the pattern of these solution surfaces can be seen in Fig.

SE   NW

1 meter

➡ Bed-parallel Echelon Thrust
     Fault Arrays
|| Bedding-Normal Veins and
     Maximum Principal Stress
     Trajectories
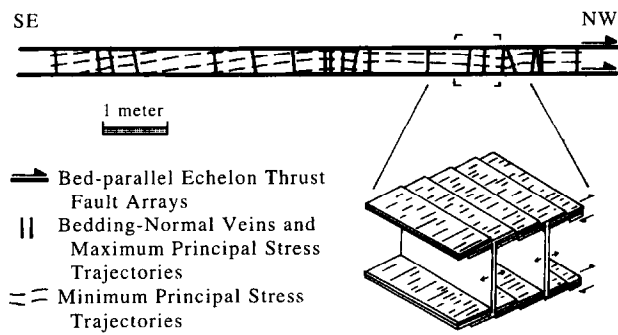≃ ≃ Minimum Principal Stress
     Trajectories

Fig. 15. Cross-section with the inferred stress trajectories from bedding-normal veins at Bays Mountain. The inferred minimum principal stress trajectories have a dashed pattern and are inclined slightly to the faults. Inset shows the relationship between bed-parallel echelon thrust fault arrays and bedding-normal veins.

5(c). In this model $\theta_r = 65°$ and $\mu = 0.0001$. Neither the local stress pattern for a contractional stepover with $\theta_r = 30°$ (Fig. 5b) nor that with $\theta_r = 80°$ (Fig. 5d) is a match. Thus, for the formation of solution surfaces in contractional stepover θ_r must be greater than 30° and less than 80°. Since both the horsetail solution surfaces and the contractional stepovers are components of the cleavages, and using the most restrictive range for θ_r, then θ_r must have been between 45° and 70°, and μ is 0.0001 for the cleavages.

Formation of structural elements between parallel faults

Veins and cleavages can be used to map the local stress field between parallel faults. Such a stress field was mapped based on a group of bedding-normal veins at Bays Mountain (Fig. 15). The bedding-normal veins parallel the orientation of the maximum principal stress trajectories (solid vertical lines in Fig. 15) and the minimum principal stress trajectories will be perpendicular to the veins, and are shown as dashed lines in the figure. The bed-parallel echelon thrust fault arrays (solid horizontal lines in Fig. 15) are simplified as continuous fault zones on the top and bottom surfaces of the cross-section but, as was discussed earlier, these zones are actually discontinuous faults connected by pull-aparts (see inset Fig. 15). As can be seen in this figure, the minimum principal stress trajectories are slightly wavy lines that roughly parallel the faults. However, near the southeast (left) end of the cross-section, the stress trajectories dip slightly (<20°) counter-clockwise relative to the trend of the echelon thrust fault arrays. By comparing principal stress patterns determined from the field data with those from the numerical models for parallel faults (Fig. 7), the coefficient of friction acting along the fault planes is estimated to be less than or equal to 0.1. Also, θ_r must be greater than 45°.

Two possible explanations are proposed for the wavy pattern and slight counter-clockwise rotation of the trajectories for the local minimum principal stress observed in Fig. 15. First, changes in the mechanical

properties along the fault planes may cause the shear strength of the faults to vary. Rundle et al. (1984) developed a model that assumes different slip properties on different sections of a fault plane. A similar variation was part of a model that included an isolated slip patch along a fault (Martel and Pollard, 1989). A model by Erickson and Wiltschko (1991) related the variation in shear strength along a fault to changes in cohesion and frictional resistance. Second, the numerical models assumed that the parallel faults are continuous. The field relationships show that the boundary faults are discontinuous, and the fault segments are connected by pull-aparts. Numerical models of parallel echelon fault arrays with extensional stepovers reveal a more complex pattern in the domain bounded by the fault arrays. This complexity results from two factors. First, the fault segments have a slight counter-clockwise rotation relative to the trend of the echelon thrust fault array (see the inset in Fig. 15). Since the fault segments are frictionless, then locally the fault segments are the principal planes. The second factor is that the length of fault segments is small relative to the length of the echelon array. The smaller the relative length of the fault segments, the closer the solution is to the two parallel faults model. The interaction of the local stress pattern due to the fault segments and the larger stress pattern due to the array may account for the variability observed in the field stress pattern.

Formation of normal faults and associated veins

Detailed mapping at the location near Holston Mountain indicates that the normal faults may form in regions bounded by intermediate thrust faults. The same pattern of normal faults bounded by intermediate thrust faults has been proposed to explain the localization of normal faults at Bays Mountain (Ohlmacher and Aydin, 1995). Thus, the normal faults may result from tension produced in the domain between two parallel thrust faults (Fig. 16) in a manner analogous to the bedding-normal veins extending the domain between two bed-parallel echelon thrust fault arrays (Fig. 15).

The frictional resistance along the normal faults presents a problem. The normal faults form in conjugate sets with the SE-dipping faults dominating. Based on the conjugate geometries of the faults, the coefficient of
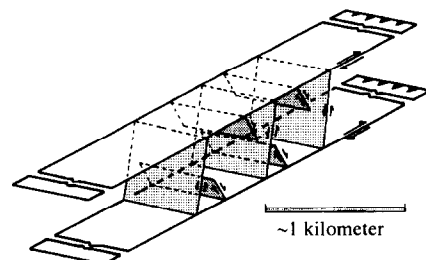

~1 kilometer

Fig. 16. Sketch of normal fault formation between two parallel intermediate thrust faults.

friction is estimated at about 0.6. This probably represents the coefficient of friction for the intact rock. However, this is probably not the coefficient of friction on the faults after the faults become established. Trajectories for the minimum principal stress were mapped based on the normal fault-subparallel veins (Fig. 13). These trajectories are perpendicular to the normal faults indicating that the normal faults are principal stress planes. Thus, after the normal faults become throughgoing planes, their coefficient of friction must drop to nearly zero.

Summary of the numerical model and field relationship comparisons

Two conclusions can be drawn from the cases presented in this section. First, from the horsetail solution surfaces, compressional stepovers and bedding-normal veins, the angle between the orientation of the remote maximum principal stress trajectory and the fault planes is greater than 45°. Second, the echelon thrust fault arrays, intermediate thrust faults and normal faults after they become established are all planes with a very low coefficient of friction. A similar result has been inferred previously using large-scale structures and local stress measurements. However, this is the first time that the associated structures have been used to demonstrate the state of stress and fault conditions on outcrop-scale faults.

DISCUSSION

Fluid pressure during deformation

In the numerical models the frictional resistance along the fault planes was controlled by adjusting the coefficient of friction. When the numerical model results state that the fault planes are nearly frictionless, it is the frictional resistance along the fault that has a value near zero. Neglecting cohesion along the fault plane, frictional resistance τ_f in a Mohr–Coulomb failure criterion is defined as:

$$\tau_f = (\sigma_n - p_f)\mu,$$

where σ_n is the normal stress acting along the fault plane, p_f is the fluid pressure and μ is the coefficient of friction. Therefore, the frictional resistance is a function of two variables: the coefficient of friction; and the effective stress controlled by the fluid pressure. For the frictional resistance to be very low, the fluid pressure must approach the magnitude of the normal stress and cause a corresponding decrease in the effective stress acting on the fault plane. Hubbert and Rubey (1959) proposed that high fluid pressures acting on overthrusts reduce the frictional resistance of the fault planes, and allow the faults to slip without exceeding the crushing strength of

the units within the thrust sheet.

Fluid pressure near the magnitude of the normal stress must be acting on the bed-parallel echelon thrust fault arrays and other thrust faults documented in this study. A minimum magnitude for the fluid pressure can be estimated using the stratigraphic column for northeastern Tennessee. The average thickness of the rock units above the Sevier Shale has been published by various authors (Campbell, 1894; Rodgers, 1953; Hardeman, 1966). Assuming average densities for the various rock types (Hatheway and Kiersch, 1982), the overburden pressure (σ_v) while the Stage 1 bed-parallel echelon thrust fault arrays were active would have been between 43 and 76 MPa, assuming that these thrust fault arrays form prior to any stacking of the thrust sheets. If, for example, the Pulaski thrust sheet had already overridden the Saltville thrust sheet, then the magnitude of the overburden pressure would have been higher. For the thrust faults to slip, the fluid pressure must have had approximately the same magnitude as the overburden pressure. At Bays Mountain, the calcite within the veins contains numerous fluid inclusions with either a single vapor phase or a vapor plus a liquid. The percentage of the vapor varies in these inclusions indicating possible fluid leakage from the fluid inclusions (E. Roedder, personal communication 1987). Thus, the fluid inclusions in the veins at Bays Mountain could not be used to confirm the fluid pressure magnitude estimated above.

Elevated fluid pressures in the host rock can also be inferred from the existence of the bedding-normal veins. The numerical models of parallel faults with low frictional resistance provide the proper stress orientation for tensile fracturing (Fig. 7e). However, if both remote principal stresses are compressive, the local minimum principal stress is also compressive. Bedding-normal veins, therefore, must be analogous to hydrofractures where fluid pressure is the driving stress (Secor, 1965).

Cycling of fluid pressure and fault friction

The domains bounded by Stage 1 bed-parallel echelon thrust fault arrays contain two contrasting structures: bedding-normal veins and a cleavage. Based on mineral fibers (Fig. 11c) and the field data presented earlier, θ_1 for the bedding-normal veins was about 90°. This stress orientation would not produce the observed cleavage. The cleavage, as discussed earlier, requires a maximum principal stress trajectory between 45° and 70°. Although these structures formed in the same domain and overlap temporally in a geological frame of reference, they indicate different states of stress. By comparing the numerical results for parallel faults with the state of stress indicated by the field relationships, it can be shown that the numerical model that is the closest match for the cleavage is when $\mu \approx 0.1$ along the bed-parallel echelon thrust faults (Fig. 7c). The model that best matches the formation of bedding-normal veins features faults with $\mu = 0.0001$ and $\theta_r > 45°$ (Fig. 7e). Note that a change in θ_r

without a change in the frictional resistance will not produce the desired state of stress between the parallel faults.

The primary factor affecting the frictional resistance along the faults is the fluid pressure. During the periods when the coefficient of friction was high, pressure solution was the dominant deformation mechanism and the cleavage was active. For $\mu > 0$, the fluid pressure was less than the normal stress acting on the fault. During the periods when $\mu = 0.0001$, fracturing was the dominant deformation mechanism, and bedding-normal veins were active. Frictionless faults occur when the fluid pressure equals or exceeds to the normal stress acting on the faults. From this it is inferred that both shear resistance and fluid pressure display cyclic character during deformation.

The rising fluid pressure and corresponding reduction in fault friction caused the bed-parallel echelon fault arrays to slip. As the faults slipped, the pull-aparts and the bedding-normal veins opened creating voids. The creation of these voids locally reduced the fluid pressure assuming that the permeability of the host material is relatively low and fluid flow could not keep pace with the porosity increase associate with fracturing. As the fluid pressure dropped and the fault friction increased, fault slip ceased. This behavior is similar to that of static and dynamic friction along faults.

The reduction of the fluid pressure within the pull-aparts and veins led to the precipitation of minerals, specifically calcite. As the fluid pressure decreases, the solubility of calcite also decreases (Berendsen, 1971). When the fluid pressure dropped within the pull-aparts and veins, the fluid supersaturated and calcite precipitated. Host rock inclusion trails within the pull-aparts and host rock fragments along the faults between adjacent pull-aparts in composite pull-apart veins (Ohlmacher and Aydin, 1995, fig. 4c & d) indicate that calcite precipitation was contemporaneous with fracturing and that fracturing occurred during multiple slip events.

The contrasting styles of deformation represented by the veins and cleavage can be explained in terms of slip and inter-slip periods of deformation. The formation of bedding-normal veins and pull-aparts were relatively rapid events and when combined with the motion of the fault probably dominated slip periods (Sibson, 1989). However, pressure solution is a relatively slow process that dominated the inter-slip period (Gratier and Gamond, 1990).

The kinematic model proposed for the contrasting deformation styles involves a periodic cycling between high fluid pressure with a corresponding lower frictional resistance and low fluid pressure with higher frictional resistance. When the fluid pressure reached a critical level, the faults slipped and fracturing dominated the deformation. During this slip period the pull-aparts and bedding-normal veins opened lowering the fluid pressure, which in turn raised the frictional resistance along the faults and allowed minerals to be precipitated in the openings. Slowly, during the inter-slip period, the fluid

pressure recovered. During this period, pressure solution dominated the deformation and the cleavage system actively formed. This model of slip and inter-slip deformation repeats itself, producing the complex temporal and spatial relationships between bedding-normal veins and cleavages observed in the domains bounded by bed-parallel echelon thrust fault arrays.

If the fluid pressure cycled with slip as is proposed above, then it could lead to seismic pumping (Sibson et al., 1975). Assuming that the hydraulic heads were greater in the hinterland than in the foreland, then, as the faults slipped and fluid pressure dropped, the regional hydraulic gradient would have produced a slight tendency for more fluids to flow into the voids from the hinterland. Ohlmacher and Aydin (1995) observed that the bed-parallel echelon thrust fault arrays with composite pull-apart veins and the bedding-normal veins form one of three fracture networks for fluid migration during the tectonic deformation. Seismic pumping may be the mechanism that moves the fluids along these fracture networks.

Overprinting of contractional and extensional structures in thrust fault terranes may be a widespread phenomenon (Harris and Milici, 1977; Coward, 1982; Platt and Leggett, 1986; Wojtal, 1986; Wojtal and Mitra, 1986; Woodward et al., 1988). Erickson and Wiltschko (1991) suggested that the formation of these overprinting patterns is due to the spatial changes in the shear strength along the fault plane. Our results show a cyclic temporal relationship between contractional and extensional structures. We relate this periodicity to changes in the shear strength caused by variations in fluid pressure along the faults.

The proposed interplay between the fluid pressure acting on a fault and the friction along the fault together with the angle between the remote stresses and the fault planes in the arrays of thrust faults provides dramatically different orientations of the local stresses between parallel faults. For nearly frictionless faults, if the angle between the greatest compressive stress and the two parallel faults is less than 45° ($\theta_r < 45°$), then the local greatest compressive stress orientation is parallel to the faults everywhere in the domain bounded by the faults ($\theta_1 = 0°$; Fig. 17a). If the angle between the remote greatest compressive stress and the fault is larger than 45° ($\theta_r > 45°$), then the local greatest compressive stress is perpendicular to the faults ($\theta_1 = 90°$; Fig. 17b). These results are consistent with the observation that, in transtensional strike-slip environments, normal faults occur parallel to the strike-slip faults, whereas in transpressional environments thrust/reverse faults occur parallel to the strike-slip faults (Zoback and Zoback, 1991).

CONCLUSIONS

The displacement discontinuity boundary-element method was used to explain and interpret the geometry

σ_1^r σ_1^r

$\theta_1 = 0°$ $\theta_1 = 90°$

(a) $\theta_r < 45°$ (b) $\theta_r > 45°$
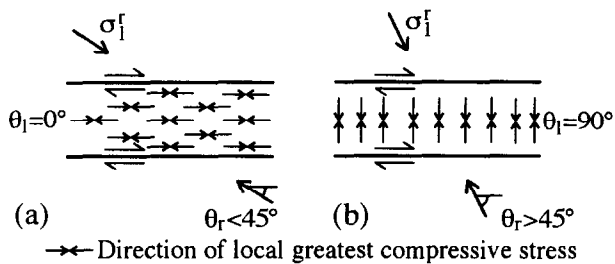
→←— Direction of local greatest compressive stress

Fig. 17. Sketches of the local state of stress in the domain bounded by two frictionless faults based on the model results (Fig. 7). (a) When the remote (applied) greatest compressive stress trajectory is oriented less than 45° to the faults, the local greatest compressive stress trajectory is parallel ($\theta_1 = 0°$) to the faults throughout the domain. (b) When the remote greatest compressive stress trajectory is oriented greater than 45° to the faults, the local greatest compressive stress trajectory is perpendicular ($\theta_1 = 90°$) to the faults throughout the domain.

and relative ages of veins and solution surfaces relative to faults observed at Bays and Holston Mountains. Numerical models of isolated faults established the relationships between these structural elements and the stress configurations in both the extensional and contractional quadrants of the faults. Models of pull-aparts between echelon faults show a decrease in the mean stress (tension) and is consistent with the observed tensile fracturing. Contractional stepover models show increased mean stress (compression) and are consistent with the observed solution surfaces.

The local stress trajectories associated with faults in these models are controlled primarily by two parameters: (1) the frictional resistance along the faults; and (2) the angle between the remote maximum principal stress orientation and the fault plane.

Within the domains bounded by bed-parallel echelon thrust fault arrays with composite pull-apart veins, a contrasting structural style exists between the cleavages and bedding-normal veins. Numerical models of parallel faults, combined with the geometric and temporal relationships between the bedding-normal veins and the faults, imply a very low frictional resistance to slip along the faults and the remote maximum principal stress oriented greater than 45° to the bed-parallel echelon thrust fault arrays. The low frictional resistance along the faults probably results from nearly lithostatic fluid pressures acting on the faults.

Contrasting these results is the cleavage that shows a complex cross-cutting relationship with the bedding-normal veins. The cleavage, which is composed of echelon thrust faults with contractional stepovers, appears to be developing in response to the remote state of stress with the orientation of the maximum principal stress trajectory between 45° and 70° to the faults. The orientation of the bedding-normal veins implies that the orientation of the maximum principal stress trajectory is at 90° to the fault planes in the same domain. A cyclic fluid pressure and shear resistance, which is similar to the notion of static and dynamic friction, explains these contrasting states of stress. During slip events the fluid

pressure was relatively high, shear resistance was decreased and fracturing dominated the deformation. During inter-slip periods the fluid pressure was relatively low and fault frictional resistance was higher, and thus pressure solution dominated the deformation. This periodic cycling between low and high fluid pressure may have moved fluids through the fractures within the Sevier Shale by seismic pumping.

Normal faults (Stage 4) that may occur between parallel intermediate thrust faults (Stage 3) may have formed in a state of stress analogous to the bedding-normal veins. Thus, the remote maximum principal stress trajectory was greater than 45° to the intermediate thrust faults and the coefficient of friction was very low. The conjugate geometry of the normal faults indicates that the coefficient of friction when these faults formed was relatively high. However, secondary veins along the normal faults indicate that the coefficient of friction is nearly frictionless after the normal faults were established.

The most significant result of this study is a direct demonstration of the effect of fault friction and remote stress orientation on the state of stress surrounding small faults and how this state of stress varies periodically depending on fluid pressure. It is shown that the faults are intermittently parallel to one of the principal stress planes. This principal stress plane may be either the maximum or the minimum principal stress depending on the angle between the faults and the remote principal stresses. This result is consistent with crustal scale fault patterns: normal faults being parallel to major strike-slip faults in transtensional regimes and thrust/reverse faults being parallel to major strike-slip faults in transpressional regimes.

REFERENCES

Anderson, M. P. and Woessner, W. W. (1992) Applied Groundwater Modeling Simulation of Flow and Advective Transport. Academic Press, San Diego.

Aydin, A. (1988) Discontinuities along thrust faults and the cleavage duplex. In Geometries and Mechanisms of Thrusting, with Special Reference to the Appalachians, eds G. Mitra and S. Wojtal, pp. 223–232. Geological Society of America Special Paper 222.

Aydin, A. and Nur, A. (1985) The types and role of stepovers in strike-slip tectonics. In Strike-slip Deformation, Basin Formation, and Sedimentation, eds K. T. Biddle and N. Christie-Blick, pp. 35–44. Society of Economic Paleontologists and Mineralogists Special Publication 37.

Aydin, A. and Schultz, R. A. (1990) Effect of mechanical interaction on the development of strike-slip faults with echelon patterns. Journal of Structural Geology 12, 123–129.

Berendsen, P. (1971) The solubility of calcite in CO_2–H_2O solutions from 100 degrees to 300 degrees C, 100 to 1000 bars, and 0 to 10 weight per cent CO_2, and geologic applications. Ph.D. dissertation, University of California, Riverside.

Broek, D. (1983) *Elementary Engineering Fracture Mechanics*. Martinus Nijhoff, Boston, Massachusetts.

Campbell, M. R. (1894) *Geologic Atlas, Estillville Folio* (No. 12). U.S. Geological Survey.

Coward, M. P. (1982) Surge zones in the Moine thrust zone of NW Scotland. *Journal of Structural Geology* **4**, 247–256.

Crouch, S. L. (1976) Analysis of stresses and displacements around underground excavations: an application of the displacement discontinuity method. University of Minnesota Geomechanics Report.

Crouch, S. L. and Starfield, A. M. (1983) *Boundary Element Methods in Solid Mechanics*. George Allen and Unwin, London.

De Paor, D. G., Simpson, C., Bailey, C. M., McCaffrey, K. J. W., Beam, E., Gower, R. J. W. and Aziz, G. (1991) The role of solution in the formation of boudinage and transverse veins in carbonate rocks at Rheems Pennsylvania. *Bulletin of the Geological Society of America* **103**, 1552–1563.

Erickson, S. G. and Wiltschko, D. V. (1991) Spatially heterogeneous strength in thrust fault zones. *Journal of Geophysical Research* **96**, 8427–8439.

Fletcher, R. C. and Pollard, D. D. (1981) Anticrack model for pressure solution surfaces. *Geology* **9**, 419–424.

Gratier, J. P. and Gamond, J. F. (1990) Transition between seismic and aseismic deformation in the upper crust. In *Deformation Mechanisms, Rheology and Tectonics*, eds R. J. Knipe and E. H. Rutter, pp. 461–473. Geological Society of London Special Publication **54**.

Hardeman, W. D. (1966) *Geologic Map of Tennessee, East Sheet*. Tennessee Division of Geology.

Harris, L.D. and Milici, R.C. (1977) Characteristics of thin-skinned style of deformation in the southern Appalachians, and potential hydrocarbon traps. *U.S. Geological Survey Professional Paper* **1018**, 1–40.

Hatheway, A. W. and Kiersch, G. A. (1982) Engineering properties of rock. In *Handbook of Physical Properties of Rock*, ed. R. S. Carmichael, pp. 290–331. CRC Press, Boca Raton, Florida.

Hubbert, M. K. and Rubey, W. W. (1959) Role of fluid pressure in mechanics of overthrusting: I Mechanics of fluid-filled porous solids and its application to overthrust faulting. *Bulletin of the Geological Society of America* **70**, 115–166.

Jessell, M. W., Willman, C. E. and Gray, D. R. (1994) Bedding parallel veins and their relationship to folding. *Journal of Structural Geology* **16**, 753–767.

Kanninen, M. F. and Popelar, C. H. (1985) *Advanced Fracture Mechanics*. Oxford University Press, New York.

Kulander, B. R. and Dean, S. L. (1986) Structure and tectonics of Central and Southern Appalachian Valley and Ridge and Plateau Provinces, West Virginia and Virginia. *Bulletin of the American Association of Petroleum Geologists* **70**, 1674–1684.

Lawn, B. R. and Wilshaw, T. R. (1975) *Fracture of Brittle Solids*. Cambridge University Press, Cambridge.

Martel, S. J. and Pollard, D. D. (1989) Mechanics of slip and fracture along small faults and simple strike-slip fault zones in granitic rock. *Journal of Geophysical Research* **94**, 9417–9428.

Mount, V. S. and Suppe, J. (1987) State of stress near the San Andreas fault: Implications for wrench tectonics. *Geology* **15**, 1143–1146.

Nickelsen, R. P. (1986) Cleavage duplexes in the Marcellus Shale of the Appalachian foreland. *Journal of Structural Geology* **8**, 361–371.

Ohlmacher, G. C. and Aydin, A. (1995) Progressive deformation and fracture patterns during foreland thrusting in the southern Appalachians. *American Journal of Science* **295**, 943–987.

Platt, J. P. and Leggett, J. K. (1986) Stratal extension in thrust footwalls, Makran accretionary prism: implications for thrust tectonics. *Bulletin of the American Association of Petroleum Geologists* **70**, 191–203.

Pollard, D. D. and Segall, P. (1987) Theoretical displacements and stresses near fractures in rock: with applications to faults, joints, dikes and solution surfaces. In *Fracture Mechanics in Rock*, ed. B. K. Atkinson, pp. 277–349. Academic Press, San Diego.

Ramsay, J. G. and Huber, M. I. (1983) *The Techniques of Modern Structural Geology. Volume 1: Strain Analysis*. Academic Press, London.

Reade, T. M. (1908) The mechanics of overthrusts. *Geological Magazine* **5**, 518.

Rice, J. R. (1992) Fault stress states, pore pressure distributions, and the weakness of the San Andreas fault. In *Fault Mechanics and Transport Properties of Rock*, eds B. Evans and T. F. Wong, pp. 475–503. Academic Press, London.

Rodgers, J. (1949) Evolution of thought on structure of middle and southern Appalachians. *Bulletin of the American Association of Petroleum Geologists* **33**, 1643–1654.

Rodgers, J. (1953) *Geologic Map of East Tennessee, with Explanatory Text*, Vol. 58, Part 2. Bulletin of the Tennessee Division of Geology.

Rodgers, J. (1970) *The Tectonics of the Appalachians*. John Wiley and Sons, New York.

Rundle, J. B., Kanamori, H. H. and McNally, K. C. (1984) An inhomogeneous fault model for gaps, asperities, barriers, and seismicity migration. *Journal of Geophysical Research* **89**, 10219–10231.

Secor, D. T. (1965) Role of fluid pressure in jointing. *American Journal of Science* **263**, 633–646.

Segall, P. and Pollard, D. D. (1980) Mechanics of discontinuous faults. *Journal of Geophysical Research* **85**, 4337–4350.

Sibson, R. H. (1989) Earthquake faulting as a structural process. *Journal of Structural Geology* **11**, 1–14.

Sibson, R. H., Moore, J. M. M. and Rankin, A. H. (1975) Seismic pumping—a hydrothermal transport mechanism. *Journal of the Geological Society of London* **131**, 653–659.

Smoluchowski, M. S. (1909) Some remarks on the mechanics of overthrusts. *Geological Magazine* **6**, 204–205.

Wojtal, S. (1986) Deformation within foreland thrust sheets by populations of minor faults. *Journal of Structural Geology* **8**, 341–360.

Wojtal, S. and Mitra, G. (1986) Strain hardening and strain softening in fault zones from foreland thrusts. *Bulletin of the Geological Society of America* **97**, 674–687.

Woodward, N. B. and Gray, D. R. (1985) Southwest Virginia, Tennessee, and northern Georgia. In *Valley and Ridge Thrust belt: Balanced Structural Sections, Pennsylvania to Alabama*, ed. N. B. Woodward, pp. 40–53. *Studies in Geology*. University of Tennessee, Department of Geological Sciences, **1**.

Woodward, N. B., Wojtal, S., Paul, J. B. and Zadins, Z. Z. (1988) Partitioning of deformation within several external thrust zones of the Appalachian orogen. *Journal of Geology* **96**, 351–361.

Zoback, M. D. and Zoback, M. L. (1991) Tectonic stress field of North America and relative plate motions. In *Neotectonics of North America* eds D. B. Slemmons, E. R. Engdahl, M. D. Zoback and D. D. Blackwell, pp. 339–366. Decade Map Vol. Geological Society of America, **1**.

Zoback, M. D., Zoback, M. L., Mount, V. S., Suppe, J., Eaton, J. P., Healy, J. H., Oppenheimer, D., Reasenberg, P., Jones, L., Raleigh, C. B., Wong, I. G., Scotti, O. and Wentworth, C. (1987) New Evidence on the state of stress of the San Andreas fault system. *Science* **238**, 1105–1111.